HHS Public Access

Author manuscript

Mol Cancer Ther. Author manuscript; available in PMC 2020 May 01.

Published in final edited form as:

Mol Cancer Ther. 2019 November ; 18(11): 2074–2084. doi:10.1158/1535-7163.MCT-18-0354.

Tumor priming by SMO inhibition enhances antibody delivery and efficacy in a pancreatic ductal adenocarcinoma model

Jun Wang[1], **Darren K.W. Chan**[1], **Arindam Sen**[2,3], **Wen Wee Ma**[4,†], **Robert M. Straubinger**[1,3,5,*]

[1]Department of Pharmaceutical Sciences, University at Buffalo, State University of New York, Buffalo, New York

[2]Physiology and Biophysics, University at Buffalo, State University of New York, Buffalo, New York

[3]Department of Cell Stress Biochemistry and Biophysics, Roswell Park Comprehensive Cancer Center, Buffalo, New York

[4]Department of Medicine, Roswell Park Comprehensive Cancer Center, Buffalo, New York

[5]Department of Pharmacology and Therapeutics, Roswell Park Comprehensive Cancer Center, Buffalo, New York

Abstract

Despite frequent overexpression of numerous growth factor receptors by pancreatic ductal adenocarcinomas (PDAC), such as Epidermal Growth Factor Receptor (EGFR), therapeutic antibodies have not proven effective. Desmoplasia, hypovascularity, and hypoperfusion create a functional drug delivery barrier that contributes to treatment resistance. Drug combinations that target tumor/stroma interactions could enhance tumor deposition of therapeutic antibodies, although clinical trials have yet to support this strategy. We hypothesize that macromolecular- or nanoparticulate therapeutic agents may best exploit stroma-targeting ‘tumor priming’ strategies, based on the fundamental principles of the Enhanced Permeability and Retention (EPR) phenomenon. Therefore, we investigated the molecular and pharmacological tumor responses to NVP-LDE225, a SMO inhibitor of sonic hedgehog signaling (sHHI), of patient-derived xenograft models that recapitulate the desmoplasia and drug delivery barrier properties of PDAC. Short-term sHHI exposure mediated dose- and time-dependent changes in tumor microvessel patency, extracellular matrix architecture, and interstitial pressure, which waned with prolonged sHHI exposure, and increased nanoparticulate permeability probe deposition in multiple PDAC PDX isolates. During sHHI-mediated priming, deposition and intra-tumor distribution of both a non-targeted monoclonal antibody (mAb) and a mAb targeting EGFR, cetuximab, were enhanced. Sequencing the sHH inhibitor with cetuximab administration resulted in marked tumor growth inhibition compared to cetuximab alone. These studies suggest that PDAC drug delivery barriers confound efforts to employ mAb against targets in PDAC, and that short-term, intermittent exposure to stromal modulators can increase tumor cell exposure to therapeutic antibodies,

[*]**Corresponding Author:** Robert M. Straubinger, Department of Pharmaceutical Sciences, University at Buffalo, State University of New York, Buffalo, New York 14214, Tel: (716) 645-2844, rms@buffalo.edu.

[†]Current Address: Department of Medical Oncology, Mayo Clinic, Rochester, Minnesota 55905

Conflict of interest: The authors declare no potential conflicts of interest.

improving their efficacy, and potentially minimize adverse effects that may accompany longer-term, continuous sHHI treatment.

Keywords

Pancreatic ductal adenocarcinoma; drug delivery; Sonic Hedgehog signaling; NVP-LDE225; cetuximab; sequential drug combination; interstitial fluid pressure; hyaluronic acid; collagen I

Introduction

Pancreatic cancer is the fourth most common cause of cancer mortality in the United States (1). Pancreatic ductal adenocarcinoma (PDAC) is the most prevalent, and has a dismal 5-year survival of 6%. Chemotherapy provides only marginal therapeutic benefit (1,2), and several factors conspire to limit its efficacy. Extensive expansion of extracellular matrix (ECM) and stromal cells creates a barrier to drug delivery (3–5), and inadequate drug exposure of tumor cells is a key contributor to therapeutic failure. In addition, PDAC tumors are hypovascular and hypoperfused, which, along with high interstitial fluid pressure (IFP) and tumor solid stress, limits drug delivery (5–10).

Drug delivery barriers in PDAC hinder tumor access of macromolecules such as monoclonal antibodies (mAb) to a greater extent than small-molecule drugs. Following convective delivery to the tumor *via* the blood, mAb must extravasate and then distribute throughout the tumor. Diffusion rates of macromolecules in tissues are far lower than those of small molecule drugs, and the extensive ECM produced by stromal cells constitutes a physical barrier to intratumor distribution (5,7,11). These factors together hinder establishment of effective tumor concentrations of macromolecular drugs. Notably, delivery of inadequate drug concentrations may exacerbate treatment resistance by selecting for therapy-resistant cells (12,13).

Strategies that target signaling pathways supporting stromal elaboration represent a potential approach to compromise the drug delivery barriers in PDAC. Sonic hedgehog (sHH) signaling promotes proliferation of tumor stromal cells and stimulates synthesis of ECM, which hinders drug penetration (4,14–17). Effects of sHH signaling upon tumor microvessel density and angiogenesis are complex. Reports indicate that sHH signaling promotes angiogenesis (18–21), and that Smoothened (SMO) inhibitors of sHH signaling (sHHI) mediate transient elevation of tumor microvessel density, perfusion, permeability, as well as delivery of chemotherapeutic agents (4) and nanoparticulate drug carriers (22). The effects of sHH signaling inhibition appear to be dose-dependent, with partial inhibition increasing both tumor growth and the angiogenic influence of tumor-associated fibroblasts, whereas complete inhibition reduces tumorigenesis and angiogenesis (23). Contrasting observations suggest that stroma restrains tumor growth (24–26), and led us to hypothesize that optimal selection of the dose and duration of sHHI treatment may be essential for successful deployment of sHHI to target tumor drug delivery barriers.

Our objective was to test the hypothesis that a temporal “tumor priming” window, established by sHHI pretreatment, could compromise the barrier to therapeutic mAb

deposition by increasing tumor perfusion and enhancing intra-tumor distribution. Numerous sHHIs have been developed, and two are clinically approved. NVP-LDE225 (Sonidegib, Novartis) was chosen for these studies (27). Because most cell-line based pancreatic cancer models lack the desmoplasia typical of PDAC, patient-derived xenograft (PDX) PDAC models were selected that recapitulate the desmoplasia and low vascularity of human PDAC (28). Cetuximab was chosen as the proof-of-concept tumor-targeting mAb because approx. 85% of PDAC tumors overexpress the epidermal growth factor receptor (EGFR) (29). Erlotinib, a small-molecule EGFR tyrosine kinase inhibitor, is approved for PDAC treatment and validates the concept of EGFR signaling as a therapeutic target (30,31). However, cetuximab has not shown efficacy in Phase III PDAC trials (32). Our approach was to assess not only the magnitude by which tumor priming can enhance mAb delivery and intra-tumor distribution, but also whether priming increases mAb antitumor efficacy.

Materials and Methods

Tumor model

PDX PaCA tumors were established at Roswell Park Comprehensive Cancer Center (28). Fragments (8mm^3) from donor mice (passages 4–9) were implanted subcutaneously in the abdominal wall of anesthetized 18–20 gm CB17 SCID mice. When tumors reached 150–500 mm^3 mice were randomized into groups having statistically indistinguishable starting volumes (Kruskal-Wallace test with Dunn's multiple comparisons test), and treatments were initiated. Tumor volume was calculated as:

$$Tumor\ volume = \frac{\text{length} \times \text{width} \times \text{depth}}{2}$$

All procedures were approved by the Roswell Park Institutional Animal Care and Use Committee. Tumor DNA sequencing for driver mutation analysis was performed by Omniseq, Inc. (Buffalo, NY) and the data have been deposited in the Sequence Read Archive of the National Center for Biotechnology Information, U.S. National Library of Medicine as BioProject Accession #PRJNA554899, https://www.ncbi.nlm.nih.gov/bioproject/PRJNA554899.

Drugs and treatment

NVP-LDE225 (Novartis), obtained as a gift or purchased as the diphosphate salt (ChemieTek, Indianapolis, IN), was formulated in 0.5% methylcellulose/0.5% Tween80 (ThermoFisher, Waltham, MA) (33) and administered daily by oral gavage. Cetuximab (anti-EGFR) and non-targeted mAb rituximab (anti-CD20) were obtained from a pharmacy. Dr. J. Balthasar (UB) provided non-targeted mAb 8C2 (anti-topotecan).

Antibody labeling

Antibodies were labeled with N-hydroxysuccinimidyl esters of Alexa Fluor 350 or 647 (ThermoFisher) according to manufacturer's instructions. Unconjugated dye was removed by dialysis and Centriprep Filter Units (30K NMWL, EMD Millipore, Billerica, MA). The final fluorophore:mAb ratio was approx. 6:1.

Immunohistochemistry and immunofluorescence

EGFR and phospho-EGFR (pEGFR) expression was detected by immunohistochemistry in paraffin-embedded tumor sections fixed in fresh 4% paraformaldehyde. Primary antibodies were anti-EGFR (ab2430, Abcam, Cambridge MA) and anti-pEGFR (#2235, Cell Signaling Technology, Danvers, MA). After deparaffinization and rehydration, antigen was retrieved in Tris/EDTA (10mM/1mM) pH 9 buffer at 95–100°C for 20–30 min. Slides were blocked (1h, 18°C) with Tris-buffered saline (TBS) containing 10% normal goat serum (NGS) and 1% bovine serum albumin. Primary antibody (1:400 anti-EGFR; 1:100 anti-pEGFR) in blocking buffer was incubated overnight at 4°C. The secondary antibody was the Vectastain elite ABC system for rabbit IgG (Vector Laboratories, Burlingame CA), used *per* manufacturer's protocols.

CD31, Ki67, and collagen I were quantified in frozen sections by immunofluorescence. Fixatives were zinc formalin (Sigma-Aldrich, St. Louis, MO) for CD31, and cold acetic acid/ethanol for Ki67 and collagen I. After blocking with Dulbecco's phosphate-buffered saline (PBS) containing 10% NGS for 1h, primary antibody dilutions (1:30 anti-CD31 #550274, BD Biosciences, San Jose, CA; 1:200 anti-collagen I ab34710, Abcam; 1:300 anti-Ki67 ab15580, Abcam) were incubated at 4°C overnight. Secondary antibodies were DyLight-649-labeled anti-rat IgG for CD31 (#072-05-16-06, KPL Inc., Gaithersburg, MD) and AlexaFluor 488-conjugated anti-rabbit IgG H&L (ab150073, Abcam) for collagen I and Ki67. Slides were mounted with proLong gold anti-fade reagent with DAPI (ThermoFisher).

Frozen sections for evaluation of hyaluronan (HA) content were fixed with acetic acid/ethanol and probed with biotinylated hyaluronic acid binding protein (#385911, EMD Millipore) and DyLight-488 streptavidin (Vector) (34).

Functional vessel density was quantified by i.v. injection of 100μg FITC-labeled *Lycopersicon esculentum* lectin (FL-1171, Vector) at 2mg/ml 10 min before euthanasia. Tumor cell:microvessel distance was measured as the average distance from each microvessel ($CD31^+$ endothelial cells) to the five nearest tumor cells (4) for all microvessels in 5 microscopic tumor fields per animal.

Quantitative Real Time-PCR

Tumor RNA was isolated *per* the manufacturer's instructions (RNeasy Minikit; Qiagen, Germantown, MD) using RNase inhibitor N808–0119 (Applied Biosystems, Waltham, MA) and kit 4368814 (Applied Biosystems) for reverse transcription (RT). Real-time polymerase chain reaction (PCR) utilized TaqMan primer probe sets in Master Mix buffer (Applied Biosystems) and an Mx3005p qPCR system (Stratagene, Waltham, MA). The primer sets were Hs01110766_m1 and Mm00494645_m1 for human and mouse Gli1, and Hs00375863_m1 and Mm00496299_m1 for human and mouse TATA box binding protein-associated factor (Applied Biosystems). Expression levels were normalized by total RNA.

Image analysis

A Zeiss AxiophotZ1 fluorescence microscope (Thornwood, NY) was used for quantitative imaging, using a 20x objective to acquire images. Analysis employed ImageJ v.1.47v (http://

rsbweb.nih.gov/ij/). Five to 7 fields were selected randomly from each section using an automated stage. A differential interference contrast (DIC) image was taken with each fluorescence field to permit image segmentation. Cetuximab and Ki67 data were normalized by the number of $DAPI^+$ nuclei per field. HA and collagen I were normalized by the stromal area/field.

Tumor IFP measurement

Tumor IFP was measured as described (35) using a pressure transducer (SPR524; Millar Instruments, Houston TX) hydraulically coupled to a 23½-gauge needle catheter and calibrated using a manometer over the range of 0–30cm water. The needle was inserted into the tumor under anesthesia and the pressure was allowed to equilibrate. Because IFP increases from the tumor periphery to the core, measurements were made at increasing depths, and the highest measured pressure was recorded.

Results

PDX tumor response to SMO antagonist treatment

Desmoplasia is a prominent characteristic of PDAC that hinders drug penetration and intra-tumor distribution. Most PDAC models of cell-line origin lack desmoplastic stroma, which potentially contributes to discrepancies between preclinical and clinical outcomes (4,36). Low-passage PDAC PDX tumors were evaluated for their retention of desmoplastic stroma and recapitulation of features of the original patient tumor through passage in immunocompromised mice ((28), Supplemental Figure S1). Supplemental Table S1 reports mutation profiles for these models. The median microvessel density (MVD) for representative PDAC PDX tumors having moderate to dense stroma was 10.4 (tumor #18254), 26.6 (#12459), 40.0 (#14312), and 63.7 (#18269) microvessels/mm^2. The microvessel-to-tumor cell distance is low in cell-line PDAC models but high in clinical PDAC (4). The average distance of the most vascularized PDAC PDX (#18269) was 20–60 μm (Fig. 1A), similar to clinical PDAC tumors (4).

Treatment of PDAC tumor-bearing mice with SMO antagonists suppresses Gli1 transcription factor expression, compromises stromal integrity, and increases drug delivery (4,15,18,22). Gli1 was therefore selected as a sHH signaling biomarker (27,37) and evaluated in numerous PDAC PDX tumors in sHHI-treated animals using species-specific TaqMan qRT-PCR probes to differentiate stromal Gli1 expression (mouse) *vs.* adenocarcinoma *GLI1* (human) expression. Little human *GLI1* was detected in these PDAC PDX tumors, and its abundance changed slightly with SMO antagonist dosing (Fig. S2). Previous reports suggest that *GLI1* expression is regulated independently of sHH signaling in most PDAC tumors having *KRAS* gene mutations (38,39). In contrast, murine *Gli1* expression was abundant, and all PDX tumors responded to 40 and 80 mg/kg/day NVP-LDE225 with time-dependent *Gli1* suppression (Fig. 1B, S2B, S3). Within 3 days of initiating daily oral dosing at 40 mg/kg/day, a dose that did not inhibit tumor growth significantly with short treatment courses (22), tumor *Gli1* expression was reduced to 5% of control at the time of plasma drug trough concentrations (24h; Fig. 1B), and inhibition was sustained through 7d of dosing. On the 10^{th} day of dosing, *Gli1* expression at the plasma trough time had recovered slightly,

suggesting onset of pharmacodynamic tolerance to continuous dosing, but the trend was not significant. Forty-eight hours after the last sHHI dose, *Gli1* expression recovered to pretreatment levels.

The time-dependent enhancement of tumor perfusion/permeability mediated by sHHI was investigated in several of the PDX PDAC models using 80nm fluorescent nanoparticles as permeability probes (22). To varying degrees, most tumors showed time-dependent changes in nanoparticle deposition after 4–7 days of daily oral sHHI dosing (Fig. S4).

PDX #18269, which has extensive desmoplasia (Fig. S1) and low vascular permeability (22) was selected for more detailed investigation of tumor responses to sHHI treatment. Effects upon cell proliferation (KI67 expression) in tumor and stromal regions were investigated by immunostaining over 20d of sHHI dosing (Fig. 1E). Tumor cell regions contained the greatest abundance of proliferating cells; in control animals, 52% of cells were $Ki76^+$ (Fig. 1C), with some regions 100% positive. Stromal regions were low in proliferation, averaging 13% $Ki67^+$ cells (Fig. 1D). For both tumor and stromal regions, treatment with sHHI reduced the number of proliferating cells. In stromal regions, the fraction of $Ki67^+$ cells decreased significantly after 3d of treatment and remained suppressed through 20d of sHHI dosing (Fig. 1D). In tumor cell regions, proliferation was statistically unchanged after 3d of treatment, but declined after 7–8d, and regions having high fractions of proliferating tumor cells became less abundant (Fig. 1C). The delayed response suggested an indirect effect of sHHI treatment upon tumor cell proliferation.

Effect of sHHI on total- and functional tumor microvessels

The hypovascularity and poor perfusion of PDAC tumors limits delivery of small-molecule drugs, and previous reports indicated that sHH signaling inhibition increased PDAC microvessel density and permeability in a time- and dose-dependent manner (4). During 10d of dosing with 40 mg/kg/day NVP-LDE225, CD31 staining showed no significant change in MVD in PDX #18269 (Fig. 2A, Fig. S5A–B). Total microvessel density does not necessarily reflect tumor perfusion, because of vascular tortuosity, loss of patency, and malformations (40,41). Therefore, functional microvessels were evaluated by *i.v.* injection of fluorescent *Lycopersicon esculentum* lectin 10 min before sacrifice. After 3d of sHHI treatment at 40 mg/kg/day, functional MVD was unchanged relative to controls (Fig. 2B), but more than doubled after 7d of treatment (Fig. 2B). In addition, the fraction of microvessels that were functional also was elevated on d7 of treatment (Fig. 2C). After 10d of treatment, when qRT-PCR analysis showed a slight recovery of *Gli1* expression (Fig. 1B), the number of functional microvessels had declined to levels statistically indistinguishable from controls. However, the fraction of functional microvessels remained elevated on d10 and on the 4 days after withdrawal of the sHHI (Fig. 2C; $p \leq 0.001$), suggesting a delay in restoration of tumor barrier properties after cessation of treatment.

The dose-dependence of sHHI effects on functional vessel abundance also was investigated. With 80mg/kg/day NVP-LDE225, functional vessel density increased transiently and earlier than with 40mg/kg/day, peaking and then declining after 3d of dosing (Fig. S5C–D). Overall, the elevation of functional vessel density with higher sHHI doses was shorter in duration.

Effect of sHHI on tumor interstitial pressure

Desmoplasia not only creates a physical drug delivery barrier, but also contributes to elevated tumor IFP and tissue solid stress (5–7). Intra-tumor pressures can collapse vessels and cause outward convective flow that could hinder antibody deposition (6,8–10). Daily sHHI treatment with 40mg/kg/day resulted in a significant ($p \leq 0.05$) decline in peak IFP at d3, which continued to decline over 11d of dosing, when it reached a nadir (Fig. 3A). Temporally, the decline in IFP appeared to precede the changes observed in functional microvessel density (Fig. 4). Doubling the sHHI dose did not reduce IFP further (Fig. S6).

Temporal modulation of the tumor ECM by sHHI treatment

Although SMO antagonists have been reported to mediate stromal thinning in PDAC, it is unclear as to how desmoplastic components respond dynamically to treatment. Therefore, effects upon the ECM components collagen I and hyaluronan were investigated. Collagen I expression is abundant in PDAC, contributing to the drug delivery barrier and also playing a role in metastasis and drug resistance (7,8,11,42,43). Whereas the collagen I network appeared as extended, thick, fiber-like structures in stromal regions of control tumors, fibers were thinner and shorter after 7d of sHHI treatment (Fig. 3B). Within 3d of initiating sHHI treatment, collagen I decreased significantly ($p \leq 0.05$) and reached a nadir on d8 (Fig. 3C).

The hyaluronan network constitutes a more dynamic component of the tumor ECM and is associated with high interstitial pressures in PDAC (6). Hyaluronic acid synthase 2, a key enzyme in HA synthesis, is regulated by the sHH signaling pathway (16). Daily sHHI treatment reduced HA abundance significantly within 3d (Fig. 3D,E; $p \leq 0.05$), and it reached a nadir after 8–10d. In particular, the regions of greatest HA abundance became less prevalent with sHHI treatment (Fig. 3E). Variability in the data increased after 10–20d of continuous dosing, suggesting possible onset of sHHI tolerance. Temporally, the changes in hyaluronan and collagen 1 paralleled the decrease in tumor IFP, which appeared to coincide with reperfusion of the tumor microvasculature (Fig. 4).

Effect of sHHI pretreatment on intra-tumor deposition of targeted and non-targeted mAb

The data together suggested that sHHI effects are dose- and time-dependent, and result in: (i) increased perfusion of the tumor *via* an increase in fraction of functional microvessels, (ii) reduced density of the stromal matrix, and (iii) reduction in tumor IFP. Therefore we investigated whether these changes correlate with changes in tumor penetration and deposition of therapeutic mAb. Cetuximab was selected as the proof-of-concept targeted mAb, owing to the prevalence of EGFR overexpression in PDAC. A non-targeted control mAb, 8C2 (anti-topotecan) was used to probe nonspecific mAb deposition.

PDX tumor #18269 expresses EGFR and showed some degree of EGFR signaling in tumor cells, based upon total- and phospho-EGFR expression (Fig. S7A,B). The targeted and non-targeted mAb were labeled with complementary, hydrophilic fluorophores, mixed, and co-administered intravenously on d7 of a 13d sHHI dosing regimen, which was designed to coincide with the time of peak functional microvessel density and the nadir of IFP, HA, and collagen I (Fig. 4). Little tumor mAb deposition was observed without sHHI priming (Fig. 5A). In contrast, cetuximab fluorescence was intense in sHHI-primed animals 12h after

mAb administration, and localized primarily with tumor cells at the stromal border. Deposition of non-targeted mAb 8C2 also increased with sHHI priming, but it was distributed throughout the tumor (Fig. S8).

The kinetics of mAb deposition and distribution were analyzed by serial sampling of control- and sHHI-pretreated mice over 7d. Tissue images were segmented into tumor and stromal regions, and mAb fluorescence intensity was quantified. The kinetics of cetuximab deposition in primed and non-primed animals were similar, but the area under the concentration-time curves (AUC) differed markedly. In both groups, cetuximab deposition in tumor cell regions peaked 12h after injection (Fig. 5B) but more than doubled in sHHI-primed mice. The similarity of cetuximab kinetics in primed *vs.* non-primed tumors, but with differences in magnitude, suggests that sHHI priming increased the tumor cell compartment accessible to mAb circulating in plasma. Deposition of the non-targeted mAb also increased with sHHI priming, but the kinetics differed from non-primed animals. With sHHI pretreatment, 8C3 concentrations showed a rapid rise (Fig. 5C), with a temporal profile similar to that of cetuximab in sHHI-primed animals, and its tumor AUC nearly doubled. In non-primed animals, 8C2 tumor concentrations increased slowly, reaching a peak ≥150h after administration. The results together demonstrate that sHHI pretreatment modulates tumor architecture so as to increase the volume of tumor that is accessible to circulating mAb, and the enhancement in deposition is not mAb-dependent.

Efficacy of cetuximab in sHHI-primed mice

Given that sHHI increased mAb access to tumor cells, we investigated the therapeutic efficacy of the sHHI/cetuximab combination. Rituximab (anti-CD20) was used as a species-matched, non-targeted control mAb. Based upon the observed temporal changes in tumor and stroma, a 14d treatment cycle was designed, in which the sHHI was administered for the first 10d, and withdrawn for the last 4d (Fig. S9). The purpose of the drug holiday was to reduce the potential for pharmacodynamic tolerance to the sHHI priming effect, which was reported to occur within 2 weeks of treatment (33), and to avoid potential adverse effects of continuous stromal inhibition (24–26). Cetuximab pharmacokinetics were analyzed using a 2-compartment model (Fig. S10A,B, Supplemental Table S2). With consideration of the temporal characteristics of tumor priming, modeling and simulation supported mAb administration on the 5^{th}, 8^{th}, and 11^{th} day of each 14d cycle. Despite the high plasma concentrations of cetuximab achieved by this dosing regimen (>10μg/mL; Fig. 6A), cetuximab had no effect upon tumor volume progression in non-primed animals (Fig. 6A, S11). In striking contrast, sHHI pretreatment combined with cetuximab retarded tumor volume progression as treatment cycles continued. Rituximab with sHHI was no more effective than the vehicle control. Tumor volume in sHHI-primed animals treated with cetuximab followed an undulating pattern that became apparent after the third treatment cycle. Upon withdrawal of the sHHI, tumor volume rebounded, despite the fact that the 3^{rd} cetuximab injection of each cycle resulted in the highest plasma mAb concentrations (Fig. 6A). Resumption of sHHI dosing after the drug holiday resulted in an immediate decline in tumor volume that was not observed in the absence of co-administered cetuximab.

Only sHHI alone and combined sHHI/cetuximab significantly extended survival to a tumor volume limit (TVL) of 2000 mm^3 (Fig. 6B). For most groups (vehicle control, cetuximab alone, rituximab±sHHI), median survival to TVL was approx. 43 days. For the sHHI alone, median survival to TVL was 67 days. Median survival to TVL for the sHHI/cetuximab regimen was 101 days, 2.4-fold greater than controls. This increase was significant compared to controls ($p \leq 0.01$) or animals treated with sHHI alone ($p \leq 0.05$).

Discussion

PDAC is a frequently-lethal cancer for which chemotherapy is seldom successful, and therapeutic antibodies have had little impact upon PDAC outcome (2,44). The numerous mechanisms of therapy resistance or failure are incompletely understood; contributing pathophysiological and molecular mechanisms include mutations in signaling pathways for growth and survival, extensive desmoplasia, and low microvessel density, perfusion, and permeability (4,6,12,13,45,46). For macromolecular agents, the dense stroma, elevated IFP, and tissue solid stress constitute key barriers interposed between the systemic circulation and delivery to tumor cells (4–7,9,10,45,47). Hypovascularity hinders convective delivery of mAb to the tumor, elevated IFP may cause an outward convective flow opposing delivery, tissue solid stress impedes interstitial diffusion of mAb after extravasation, and together, solid stress and high IFP reduce perfusion by collapsing functional microvasculature. Any strategy to enhance therapeutic antibody delivery to PDAC cells must address these barriers concurrently.

Tumor priming strategies aim to compromise the drug delivery barrier and enhance deposition of subsequently administered agent(s), and the priming approach investigated here involves interdiction of sHH signaling, which plays an important role in desmoplasia. Inhibitors of this signaling axis compromise the barriers to drug delivery by: (*i*) increasing tumor vascularity, permeability and/or perfusion, (*ii*) reducing tumor IFP and stromal integrity to reduce tissue solid stress, and (*iii*) increasing intra-tumor diffusion (4,9,16,17,19,22–24). Multiple PDAC PDX tumors responded to sHH inhibitors with a deep reduction in Gli1 transcription factor expression and increased permeability to nanoparticulate perfusion/permeability probes. One PDX model was selected for more comprehensive investigation of sHHI effects upon mAb deposition and intra-tumor distribution based upon its hypovascularity, poor permeability and perfusion, extensive desmoplasia, and detectable EGFR signaling activity. The pharmacodynamics of changes in tumor architecture and vasculature were investigated for two sHHI dose levels. Short-term treatment at a lower dose (40mg/kg/day) increased functional vessel density significantly, but total vessel density did not increase. A higher dose (80 mg/kg/day) resulted in rapid but more transient changes in functional vascularity, suggesting the importance of optimizing dose and regimen. The sHHI treatment decreased the density of the ECM constituents HA and collagen I in parallel with the reduction in IFP, relieving compression of existing vasculature, restoring perfusion, and enhancing convective delivery of antibody drugs (Fig. 4). Hydration of HA and increased collagen I elevate IFP and tissue solid stress, which consequently collapses tumor vessels (6–8). Responses of collagen I and HA to sHHI treatment were time-dependent, and suggest that the priming window for enhanced tumor cell exposure to antibody also may be transient.

The desmoplastic stroma and high intra-tumor pressures impede mAb delivery following extravasation, resulting in spatially heterogeneous intra-tumor distribution (12). Typically, mAb concentrations fall below a therapeutic threshold in regions distal to the tumor vasculature because of diffusion barriers, thereby compromising therapeutic efficacy and potentially accelerating the emergence of drug resistance (13). Priming increased the exposure of tumor cells to convective delivery, the amount of mAb deposited, and the depth of penetration.

We hypothesize that short-term exposure to SMO antagonists, interspersed with drug-free holidays, may accomplish tumor priming while minimizing onset of pharmacodynamic tolerance (33) and deleterious effects of long-term inhibition. Recent reports demonstrate that reduction in desmoplasia, or genetic ablation of sHH signaling or tumor-associated fibroblasts, promotes a more malignant, metastatic tumor phenotype (24–26). Concerns raised in an initial small-scale clinical trial of combined gemcitabine/sHHI resulted in suspension of similar trials (48). However, additional trials showed no evidence of inferiority or toxicity of the SMO antagonist treatment arms (49). Based upon pharmacodynamic analysis, 5–10d of sHHI treatment was selected here as the tumor-priming regimen for subsequent administration of cetuximab. Estimates of tumor EGFR expression (50) suggested that a dose of 7mg/kg cetuximab would constitute a saturating dose sufficient to block all accessible tumor EGFR. The kinetic data for fluorescent mAb deposition supported this prediction; the majority of the tumor bulk was not accessible to cetuximab in treatment-naïve (non-primed) animals, whereas 7d of sHHI pretreatment rendered the tumor interstitium more accessible to mAb. In primed *vs.* non-primed animals, the kinetics of cetuximab deposition were parallel, but the magnitude of deposition differed. The results suggest that tumor cell EGFR that is accessible to mAb saturates rapidly with and without priming, and that the effect of sHHI pretreatment is to increase the number of tumor cells accessible to circulating mAb.

The biodistributional effects of sHHI tumor priming upon cetuximab disposition increased therapeutic efficacy. Unsurprisingly, cetuximab in the absence of priming had no therapeutic effect in this EGFR-expressing PDX model, just as cetuximab lacks clinical activity in PDAC (32). However, repeated cycles of sHHI priming and cetuximab treatment arrested mean tumor volume progression in a fashion that was clearly dependent upon treatment with both agents. Three initial treatment cycles did not inhibit tumor volume progression perceptibly. However, in subsequent cycles, average tumor volume did not progress, despite oscillations around a mean that clearly reflected the initiation and cessation of each treatment cycle. These tumor volume oscillations represent an interesting phenomenon of undetermined underlying mechanism(s). Contributing factors likely include the timing of sHHI and mAb administration and the sHHI drug holiday. The contribution of EGFR target engagement is unclear in light of KRAS oncogenic signaling. Other possible contributions include antibody-dependent cell-mediated cytotoxicity, given that SCID mice have NK cells, neutrophils, and macrophages, and are able to respond to cetuximab (51).

Because intra-tumor mAb concentrations are far lower than required to saturate tumor EGFR, it would be important to maintain high mAb plasma concentrations during both the priming window and the drug holiday to maximize delivery. Previous studies showed that 3d

after cessation of a 10d sHHI dosing regimen, tumor permeability to 80nm nanoparticles remained elevated (22). Therefore, the d11 cetuximab dose, administered during the drug holiday, also would have access to the tumor interstitium. For most PDX models, priming effects appeared by approximately d4, and the earliest suggestion of sHHI pharmacodynamic tolerance was observed at ≥d10 of dosing; pharmacodynamic tolerance to NVP-LDE225 was reported to occur *in vitro* in as few as 13 days (33). A local nadir in tumor volume was observed mid-cycle in each of the last three treatment cycles. The rapid re-induction of tumor volume suppression upon re-initiation of sHHI treatment suggests that the 4d drug holiday restored tumor sensitivity to sHHI treatment effects. Thus a sequence of low sHHI doses, administered for the shortest interval necessary to mediate tumor priming, and interspersed with a drug holiday, may underlie success of this combination therapy strategy. The priming strategy would not be limited to cetuximab, as the data show that tumor deposition of a non-targeted, control mAb also increased during sHHI priming. These hypotheses are under investigation.

Supplementary Material

Refer to Web version on PubMed Central for supplementary material.

Acknowledgements

We thank Drs. B.L. Hylander and E.A. Repasky for advice and access to the PDAC tumor panel, R.F. Pitoniak, MSN, for curating the tumor panel, Dr. T. Roy Chaudhuri for helpful discussions, and Y. Qu and N.L. Straubinger for technical assistance. We thank Drs. L. Luus, W. Kamoun, and D.C. Drummond (Merrimack Pharmaceuticals Inc.) for sharing their unpublished MVD measurements and preliminary mutation analysis for these tumors. Novartis provided some of the NVP-LDE225. NIH/NCI grants R21CA168454 and R01CA198096 (RMS and WWM), and a grant from the UB/SUNY Center for Protein Therapeutics consortium (RMS) provided support. Comprehensive Cancer Center Support grant NIH/NCI P30CA016056 to Roswell Park provided shared resources utilized in the work. JW received partial support from an unrestricted predoctoral fellowship provided to the UB Dept. of Pharmaceutical Sciences by Genentech, Inc.

References

1. Siegel RL, Miller KD, Jemal A. Cancer Statistics, 2017. CA Cancer J Clin 2017;67:7–30. [PubMed: 28055103]
2. Vincent A, Herman J, Schulick R, Hruban RH, Goggins M. Pancreatic cancer. Lancet 2011;378:607–20. [PubMed: 21620466]
3. Bardeesy N, DePinho RA. Pancreatic cancer biology and genetics. Nat Rev Cancer 2002;2:897–909. [PubMed: 12459728]
4. Olive KP, Jacobetz MA, Davidson CJ, Gopinathan A, McIntyre D, Honess D, et al. Inhibition of Hedgehog signaling enhances delivery of chemotherapy in a mouse model of pancreatic cancer. Science 2009;324:1457–61. [PubMed: 19460966]
5. Provenzano PP, Hingorani SR. Hyaluronan, fluid pressure, and stromal resistance in pancreas cancer. Br J Cancer 2013;108:1–8. [PubMed: 23299539]
6. Provenzano PP, Cuevas C, Chang AE, Goel VK, Von Hoff DD, Hingorani SR. Enzymatic targeting of the stroma ablates physical barriers to treatment of pancreatic ductal adenocarcinoma. Cancer Cell 2012;21:418–29. [PubMed: 22439937]
7. Stylianopoulos T, Martin JD, Chauhan VP, Jain SR, Diop-Frimpong B, Bardeesy N, et al. Causes, consequences, and remedies for growth-induced solid stress in murine and human tumors. Proc Natl Acad Sci USA 2012;109:15101–8. [PubMed: 22932871]

8. Stylianopoulos T, Martin JD, Snuderl M, Mpekris F, Jain SR, Jain RK. Coevolution of solid stress and interstitial fluid pressure in tumors during progression: implications for vascular collapse. Cancer Res 2013;73:3833–41. [PubMed: 23633490]
9. Hylander BL, Sen A, Beachy SH, Pitoniak R, Ullas S, Gibbs JF, et al. Tumor priming by Apo2L/TRAIL reduces interstitial fluid pressure and enhances efficacy of liposomal gemcitabine in a patient derived xenograft tumor model. J Control Release 2015;217:160–9. [PubMed: 26342663]
10. Minchinton AI, Tannock IF. Drug penetration in solid tumours. Nat Rev Cancer 2006;6:583–92. [PubMed: 16862189]
11. Pluen A, Boucher Y, Ramanujan S, McKee TD, Gohongi T, di Tomaso E, et al. Role of tumor-host interactions in interstitial diffusion of macromolecules: cranial vs. subcutaneous tumors. Proc Natl Acad Sci USA 2001;98:4628–33. [PubMed: 11274375]
12. Tredan O, Galmarini CM, Patel K, Tannock IF. Drug resistance and the solid tumor microenvironment. J Natl Cancer Inst 2007;99:1441–54. [PubMed: 17895480]
13. Fu F, Nowak MA, Bonhoeffer S. Spatial heterogeneity in drug concentrations can facilitate the emergence of resistance to cancer therapy. PLoS Comput Biol 2015;11:e1004142. [PubMed: 25789469]
14. Lunardi S, Muschel RJ, Brunner TB. The stromal compartments in pancreatic cancer: are there any therapeutic targets? Cancer Lett 2014;343:147–55. [PubMed: 24141189]
15. Bailey JM, Swanson BJ, Hamada T, Eggers JP, Singh PK, Caffery T, et al. Sonic hedgehog promotes desmoplasia in pancreatic cancer. Clin Cancer Res 2008;14:5995–6004. [PubMed: 18829478]
16. Liu J, Li Q, Kuehn MR, Litingtung Y, Vokes SA, Chiang C. Sonic hedgehog signaling directly targets Hyaluronic Acid Synthase 2, an essential regulator of phalangeal joint patterning. Dev Biol 2013;375:160–71. [PubMed: 23313125]
17. Horn A, Palumbo K, Cordazzo C, Dees C, Akhmetshina A, Tomcik M, et al. Hedgehog signaling controls fibroblast activation and tissue fibrosis in systemic sclerosis. Arthritis Rheum 2012;64:2724–33. [PubMed: 22354771]
18. Kayed H, Kleeff J, Osman T, Keleg S, Buchler MW, Friess H. Hedgehog signaling in the normal and diseased pancreas. Pancreas 2006;32:119–29. [PubMed: 16552330]
19. Chen W, Tang T, Eastham-Anderson J, Dunlap D, Alicke B, Nannini M, et al. Canonical hedgehog signaling augments tumor angiogenesis by induction of VEGF-A in stromal perivascular cells. Proc Natl Acad Sci USA 2011;108:9589–94. [PubMed: 21597001]
20. Pola R, Ling LE, Silver M, Corbley MJ, Kearney M, Blake Pepinsky R, et al. The morphogen Sonic hedgehog is an indirect angiogenic agent upregulating two families of angiogenic growth factors. Nat Med 2001;7:706–11. [PubMed: 11385508]
21. Nakamura K, Sasajima J, Mizukami Y, Sugiyama Y, Yamazaki M, Fujii R, et al. Hedgehog promotes neovascularization in pancreatic cancers by regulating Ang-1 and IGF-1 expression in bone-marrow derived pro-angiogenic cells. PLoS One 2010;5:e8824. [PubMed: 20098680]
22. Roy Chaudhuri T, Straubinger NL, Pitoniak RF, Hylander BL, Repasky EA, Ma WW, et al. Tumor-priming Smoothened inhibitor enhances deposition and efficacy of cytotoxic nanoparticles in a pancreatic cancer model. Mol Cancer Ther 2016;15:84–93. [PubMed: 26516158]
23. Mathew E, Zhang Y, Holtz AM, Kane KT, Song JY, Allen BL, et al. Dosage-dependent regulation of pancreatic cancer growth and angiogenesis by hedgehog signaling. Cell Rep 2014;9:484–94. [PubMed: 25310976]
24. Rhim AD, Oberstein PE, Thomas DH, Mirek ET, Palermo CF, Sastra SA, et al. Stromal elements act to restrain, rather than support, pancreatic ductal adenocarcinoma. Cancer Cell 2014;25:735–47. [PubMed: 24856585]
25. Özdemir BC, Pentcheva-Hoang T, Carstens JL, Zheng X, Wu CC, Simpson TR, et al. Depletion of carcinoma-associated fibroblasts and fibrosis induces immunosuppression and accelerates pancreas cancer with reduced survival. Cancer Cell 2014;25:719–34. [PubMed: 24856586]
26. Lee JJ, Perera RM, Wang H, Wu DC, Liu XS, Han S, et al. Stromal response to Hedgehog signaling restrains pancreatic cancer progression. Proc Natl Acad Sci USA 2014;111:E3091–100. [PubMed: 25024225]

27. Pan S, Wu X, Jiang J, Gao W, Wan Y, Cheng D, et al. Discovery of NVP-LDE225, a potent and selective smoothened antagonist. ACS Med Chem Lett 2010;1:130–4. [PubMed: 24900187]
28. Hylander BL, Pitoniak R, Penetrante RB, Gibbs JF, Oktay D, Cheng J, et al. The anti-tumor effect of Apo2L/TRAIL on patient pancreatic adenocarcinomas grown as xenografts in SCID mice. J Transl Med 2005;3:22–35. [PubMed: 15943879]
29. Oliveira-Cunha M, Newman WG, Siriwardena AK. Epidermal growth factor receptor in pancreatic cancer. Cancers (Basel) 2011;3:1513–26. [PubMed: 24212772]
30. Moore MJ, Goldstein D, Hamm J, Figer A, Hecht JR, Gallinger S, et al. Erlotinib plus gemcitabine compared with gemcitabine alone in patients with advanced pancreatic cancer: a phase III trial of the National Cancer Institute of Canada Clinical Trials Group. J Clin Oncol 2007;25:1960–6. [PubMed: 17452677]
31. Faloppi L, Andrikou K, Cascinu S. Cetuximab: still an option in the treatment of pancreatic cancer? Expert Opin Biol Ther 2013;13:791–801. [PubMed: 23560505]
32. Philip PA, Benedetti J, Corless CL, Wong R, O'Reilly EM, Flynn PJ, et al. Phase III study comparing gemcitabine plus cetuximab versus gemcitabine in patients with advanced pancreatic adenocarcinoma: Southwest Oncology Group-directed intergroup trial S0205. J Clin Oncol 2010;28:3605–10. [PubMed: 20606093]
33. Buonamici S, Williams J, Morrissey M, Wang A, Guo R, Vattay A, et al. Interfering with resistance to smoothened antagonists by inhibition of the PI3K pathway in medulloblastoma. Sci Transl Med 2010;2:51ra70.
34. Lin W, Shuster S, Maibach HI, Stern R. Patterns of hyaluronan staining are modified by fixation techniques. J Histochem Cytochem 1997;45:1157–63. [PubMed: 9267476]
35. Sen A, Capitano ML, Spernyak JA, Schueckler JT, Thomas S, Singh AK, et al. Mild elevation of body temperature reduces tumor interstitial fluid pressure and hypoxia and enhances efficacy of radiotherapy in murine tumor models. Cancer Res 2011;71:3872–80. [PubMed: 21512134]
36. Korc M Pancreatic cancer-associated stroma production. Am J Surg 2007;194:S84–6. [PubMed: 17903452]
37. Wong H, Alicke B, West KA, Pacheco P, La H, Januario T, et al. Pharmacokinetic-pharmacodynamic analysis of vismodegib in preclinical models of mutational and ligand-dependent hedgehog pathway activation. Clin Cancer Res 2011;17:4682–92. [PubMed: 21610148]
38. Lauth M, Bergstrom A, Shimokawa T, Tostar U, Jin Q, Fendrich V, et al. DYRK1B-dependent autocrine-to-paracrine shift of Hedgehog signaling by mutant RAS. Nat Struct Mol Biol 2010;17:718–25. [PubMed: 20512148]
39. Nolan-Stevaux O, Lau J, Truitt ML, Chu GC, Hebrok M, Fernandez-Zapico ME, et al. GLI1 is regulated through Smoothened-independent mechanisms in neoplastic pancreatic ducts and mediates PDAC cell survival and transformation. Genes Dev 2009;23:24–36. [PubMed: 19136624]
40. Goel S, Duda DG, Xu L, Munn LL, Boucher Y, Fukumura D, et al. Normalization of the vasculature for treatment of cancer and other diseases. Physiol Rev 2011;91:1071–121. [PubMed: 21742796]
41. Xu Y, Choi J, Hylander B, Sen A, Evans SS, Kraybill WG, et al. Fever-range whole body hyperthermia increases the number of perfused tumor blood vessels and therapeutic efficacy of liposomally encapsulated doxorubicin. Int J Hyperthermia 2007;23:513–27. [PubMed: 17952765]
42. Shintani Y, Hollingsworth MA, Wheelock MJ, Johnson KR. Collagen I promotes metastasis in pancreatic cancer by activating c-Jun NH(2)-terminal kinase 1 and up-regulating N-cadherin expression. Cancer Res 2006;66:11745–53. [PubMed: 17178870]
43. Armstrong T, Packham G, Murphy LB, Bateman AC, Conti JA, Fine DR, et al. Type I collagen promotes the malignant phenotype of pancreatic ductal adenocarcinoma. Clin Cancer Res 2004;10:7427–37. [PubMed: 15534120]
44. O'Reilly EM. Adjuvant therapy for pancreas adenocarcinoma. J Surg Oncol 2013;107:78–85. [PubMed: 22886586]
45. Feig C, Gopinathan A, Neesse A, Chan DS, Cook N, Tuveson DA. The pancreas cancer microenvironment. Clin Cancer Res 2012;18:4266–76. [PubMed: 22896693]
46. Ryan DP, Hong TS, Bardeesy N. Pancreatic adenocarcinoma. N Engl J Med 2014;371:1039–49. [PubMed: 25207767]

47. Thurber GM, Schmidt MM, Wittrup KD. Factors determining antibody distribution in tumors. Trends Pharmacol Sci 2008;29:57–61. [PubMed: 18179828]

48. Ko AH, LoConte N, Tempero MA, Walker EJ, Kate Kelley R, Lewis S, et al. A Phase I Study of FOLFIRINOX Plus IPI-926, a Hedgehog Pathway Inhibitor, for Advanced Pancreatic Adenocarcinoma. Pancreas 2016;45:370–5. [PubMed: 26390428]

49. Catenacci DV, Junttila MR, Karrison T, Bahary N, Horiba MN, Nattam SR, et al. Randomized phase Ib/II study of gemcitabine plus placebo or vismodegib, a Hedgehog pathway inhibitor, in patients with metastatic pancreatic cancer. J Clin Oncol 2015;33:4284–92. [PubMed: 26527777]

50. Luo FR, Yang Z, Dong H, Camuso A, McGlinchey K, Fager K, et al. Correlation of pharmacokinetics with the antitumor activity of Cetuximab in nude mice bearing the GEO human colon carcinoma xenograft. Cancer Chemother Pharmacol 2005;56:455–64. [PubMed: 15947929]

51. Kurai J, Chikumi H, Hashimoto K, Takata M, Sako T, Yamaguchi K, et al. Therapeutic antitumor efficacy of anti-epidermal growth factor receptor antibody, cetuximab, against malignant pleural mesothelioma. Int J Oncol 2012;41:1610–8. [PubMed: 22922885]

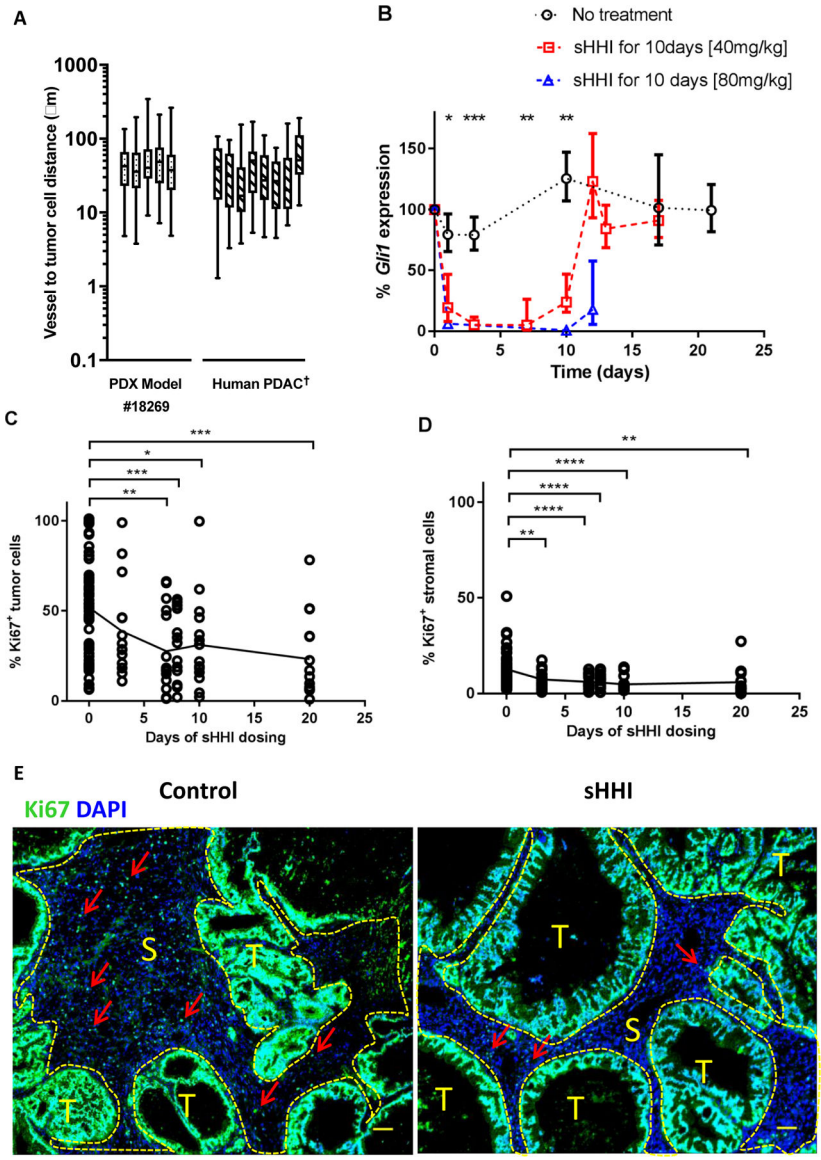

Figure 1. Characteristics of PDX model and responses to sHH inhibition

A, Microvessel-to-tumor cell distance. The distance from each $CD31^+$ microvessel to the five nearest tumor cells was measured for the PDX model #18269 and the mean value is reported. Center bar is the median, box represents range of the median 50%, and vertical bars show the minimum and maximum. †For comparison, data for human PDAC tumors are re-plotted from (4). **B-D,** asterisks indicate statistically significant differences from control, based on post hoc unpaired t test with Welch's correction for unequal sample numbers and variances: * p≤0.05; ** p≤0.01; *** p≤0.001; **** p≤0.0001; other statistical testing as indicated below. **B,** Time course of murine (stromal) *Gli1* expression inhibition by sHHI. NVP-LDE225 (40mg/kg/day) was administered *p.o.* daily to tumor-bearing mice for 10 days. One-way ANOVA: group means differ at p=0.0003. Quantification of proliferating cells during 20 days of sHHI treatment in **C,** tumor regions and **D**, stromal regions. Regions were segmented manually based on a DIC image of each fluorescence field. Each time point

consisted of n=3 mice in the sHHI treatment group and n=12 mice in the control group (time = 0). Symbols show the data for 5 random fields (20X objective) from each tumor sample in each group; C, one-way ANOVA p=0.0002; D, p=0.0001. **E,** Typical image of Ki67 proliferation antigen staining (green); cell nuclei were counterstained with DAPI (blue). The image encompasses nearly the entire tumor. (S): stromal areas outlined with yellow dashed line; (T): tumor cell regions. Red arrows: representative $Ki67^{+}$ cells in stroma. Scale bar: 100μm.

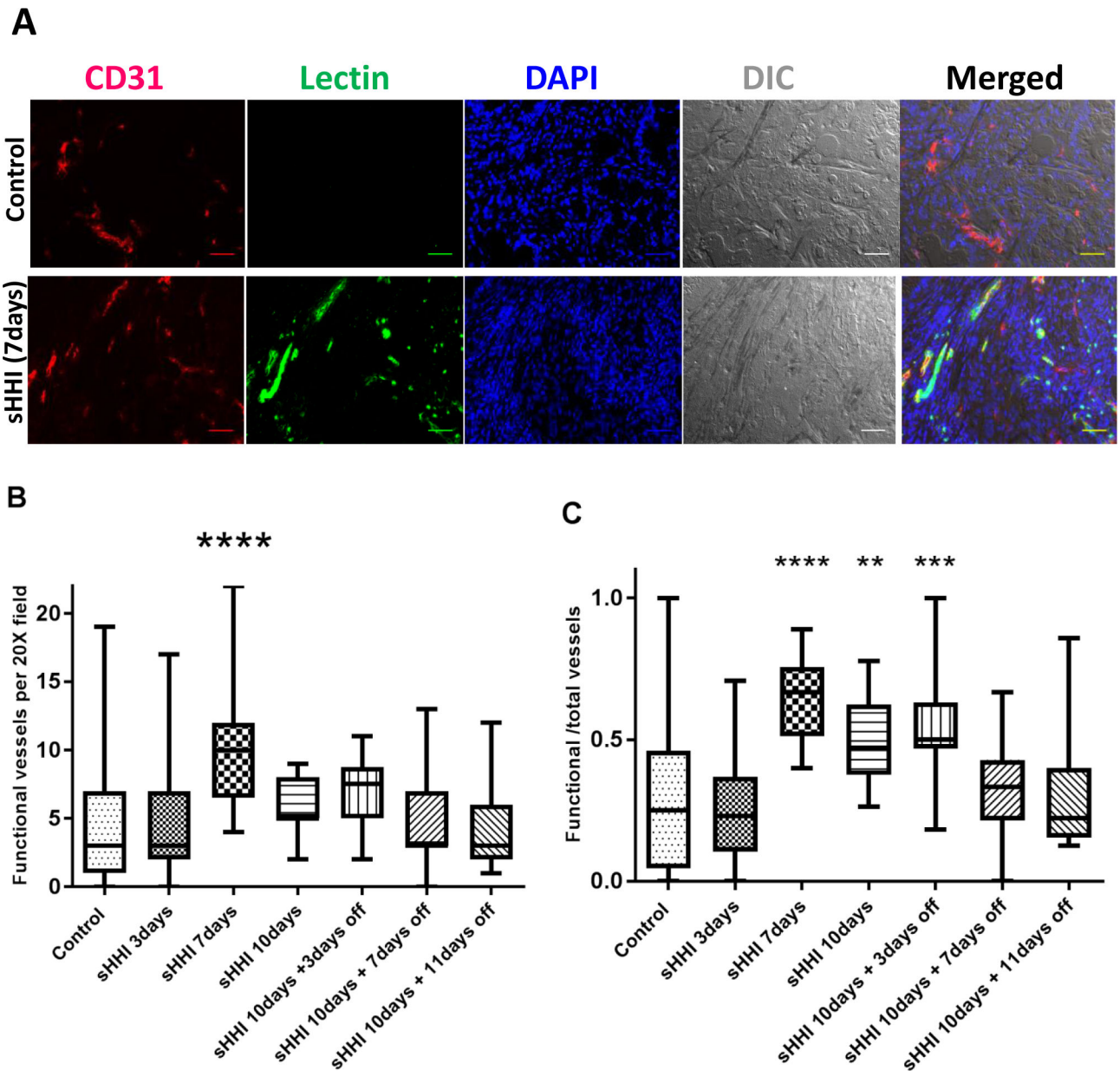

Figure 2. Effect of sHHI on tumor vascular status

Mice bearing tumor #18269 were treated daily *p.o.* for 10 days with NVP-LDE225 (40mg/kg/day) and sacrificed at intervals. Ten min before sacrifice, groups of 3 mice were injected *i.v.* with 100μg *Lycopersicon esculentum* (*Le*) lectin conjugated with FITC. **A,** Representative immunofluorescence and DIC images showing effect of sHHI on functional microvessels; CD31 staining (red) identifies total microvessels. Nuclei are counterstained with DAPI (blue). Co-staining of CD31 and *Le* lectin (green) indicates blood-perfused (functional) vessels. Control: no treatment; scale bar: 50μm. **B,** Change in number of functional vessels during the sHHI treatment; n=3 mice for each time point in the sHHI treatment group and n=9 mice in the control group. Five random fields (20X objective) were selected per tumor sample in each group. **C,** Change in the fraction of functional vessels

during sHHI treatment. Center bar is median; box represents range of median 50%; vertical bars show minimum and maximum values. Statistical analysis was by one way ANOVA with post hoc testing using Dunnett's multiple comparisons test: ** $p \leq 0.01$; *** $p \leq 0.001$; **** $p \leq 0.0001$.

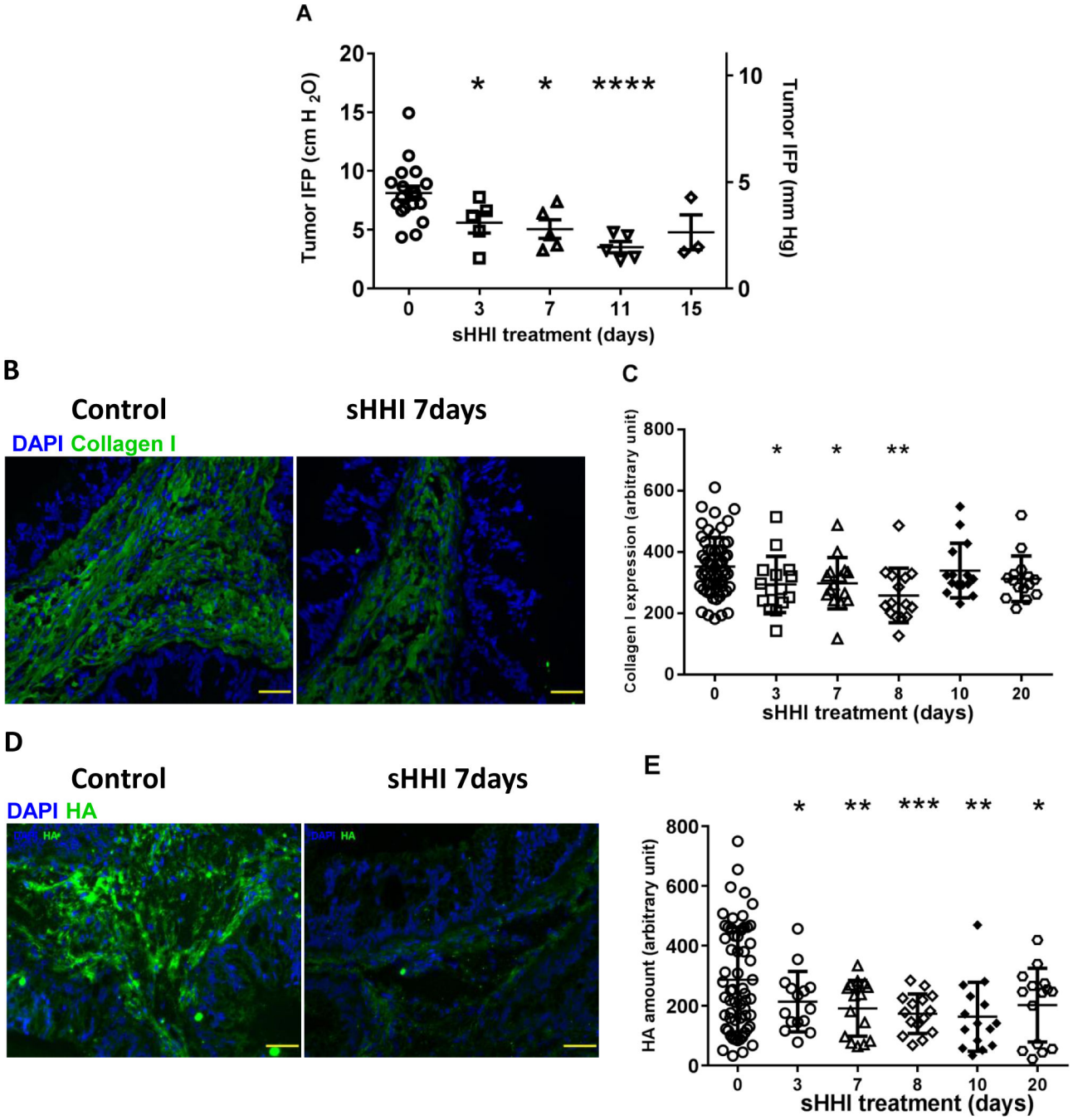

Figure 3. sHHI modulation of tumor IFP and extracellular matrix

Mice bearing tumor #18269 were treated daily for up to 20 days with sHHI (NVP-LDE225, 40mg/kg/day) as in Figure 2. At intervals, animals were sacrificed after measuring tumor interstitial pressure (*Methods*). **A,** IFP during treatment with sHHI; IFP was measured at four depths within each tumor and the peak value is reported. Each data point represents one tumor. By one-way ANOVA, group means differ at p=0.0012; asterisks: statistical differences from post hoc testing using unpaired t test with Welch's correction: * p≤0.05; ** p≤0.01; *** p≤0.001; **** p≤0.0001. **B,** Representative immunofluorescence images of

sHHI effects on collagen I (green) and on **D,** HA (green); DAPI (blue) was used as a nuclear stain; scale bar: 50μm. Quantification during sHHI treatment of **C,** collagen I (ANOVA p=0.0049; asterisks identify statistical comparisons as in panel A) and **E,** Quantification of HA (ANOVA p=0.0048; asterisks as in panel A). Quantification was based upon mean fluorescence intensity of each image. Five random fields (20X objective) were chosen per tumor with n=3 mice/point for the sHHI groups and n=12 mice for the control group.

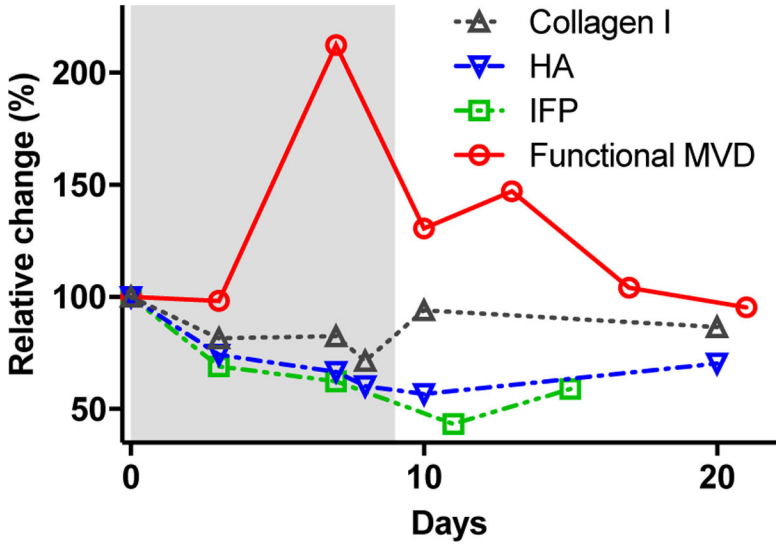

Figure 4. Mechanisms of time-dependent tumor priming by sHHI

Temporal relationships among pharmacodynamic responses during sHHI priming. Quantitative data for response endpoints shown in Figs. 2B (functional MVD), 3A (IFP), 3C (collagen 1), and 3E (hyaluronan) were normalized to their control values and replotted. Red circles: temporal changes in functional MVD over 10d of daily dosing with sHHI (grey band) were significant (Fig. 2B) on d3 ($p \leq 0.0001$). Green squares: changes in IFP over 15d of sHHI dosing were significant (Fig. 3A) at d3 ($p \leq 0.05$), d7 ($p \leq 0.05$), and d11 ($p \leq 0.0001$). Black triangles: changes in collagen I during 20d of sHHI treatment were significant (Fig. 3C) at d3 ($p \leq 0.05$), d7 ($p \leq 0.05$), and d8 ($p \leq 0.01$). Blue triangles: changes in HA with 20d sHHI treatment were significant (Fig. 3E) at d3 ($p \leq 0.05$), d7 ($p \leq 0.01$), d8 ($p \leq 0.001$), d10 ($p \leq 0.01$), and d20 ($p \leq 0.05$).

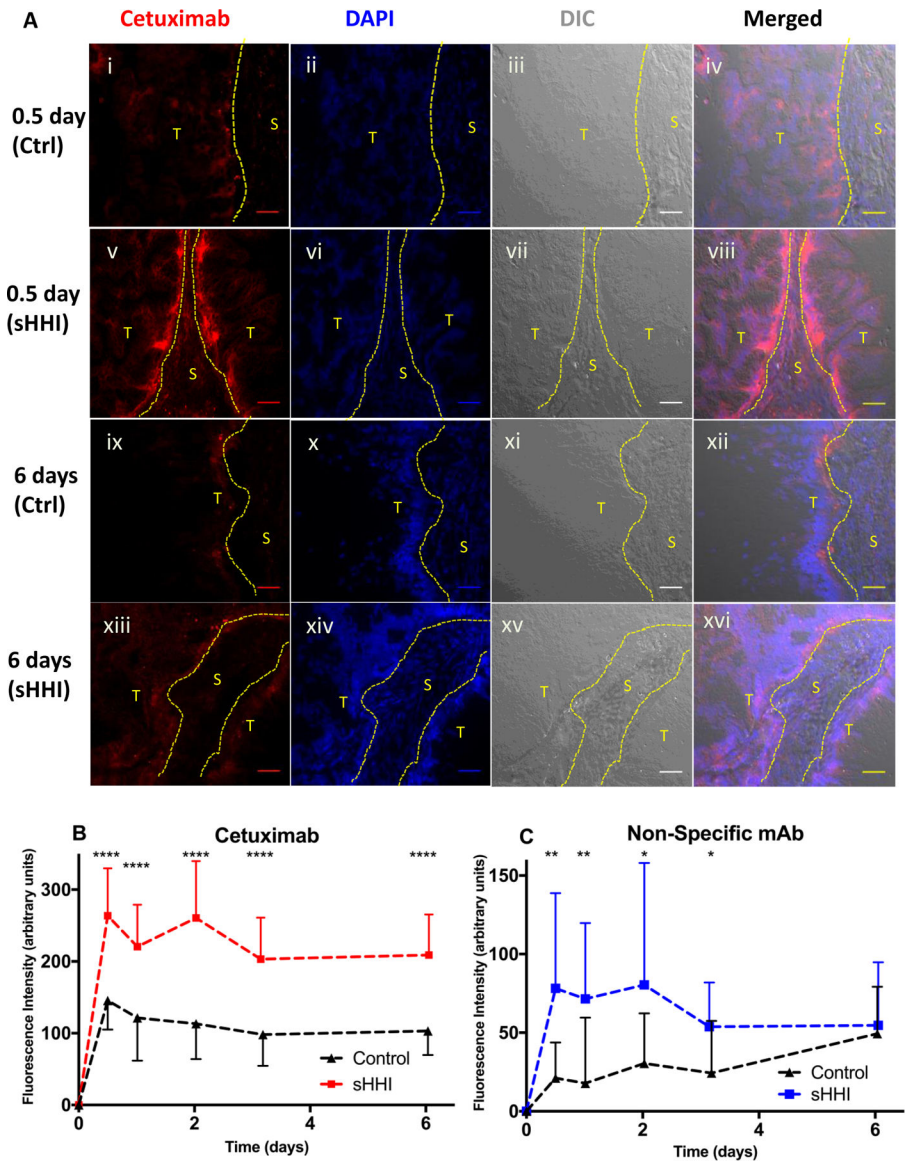

Figure 5. Effect of sHHI priming on antibody deposition in tumors

Mice bearing tumor #18269 were treated as described in Figure 2; 7 days after initiation of treatment, targeted mAb (cetuximab; 7.0mg/kg) and non-targeted mAb (8C2; 3.9mg/kg), labeled with complementary fluorophores (Alexa Fluor 647 and Alexa Fluor 350), were injected *i.v.*. Mice (n=3/group) were sacrificed at intervals. Vehicle or sHHI treatment continued throughout the experiment. Tissue sections were counterstained with DAPI and, after manually segmenting images into tumor (T) and stromal (S) regions based upon a DIC image of each field, antibody fluorescence was quantified in 5–7 random fields per section from each of 3 mice per treatment group. **A,** cetuximab deposition in tumor-cell *vs.* stromal regions 0.5 or 6 days after treatment with sHHI or vehicle. Red: Alexa Fluor 647-labeled cetuximab bound to EGFR on tumor cells. Blue: DAPI; panels i-iv: 0.5 days after cetuximab administration to controls or (v-viii) sHHI-treated animals; panels ix-xii: 6 days after cetuximab administration to controls or (xiii-xvi) sHHI-treated animals. Scale bar: 50μm. **B,**

pharmacokinetics of cetuximab deposition in tumor cell regions in control (black/triangles) and sHHI–treated (red/squares) animals. **C,** pharmacokinetics of non-targeted mAb (8C2; anti-topotecan) deposition in tumor cell areas in control (black/triangles) and sHHI-treated (blue/squares) animals. Error bar is half-sized standard deviation for clarity; symbol represents mean. Statistical analysis by unpaired t test with Welch's correction: * $p \leq 0.05$; ** $p \leq 0.01$; *** $p \leq 0.001$; **** $p \leq 0.0001$.

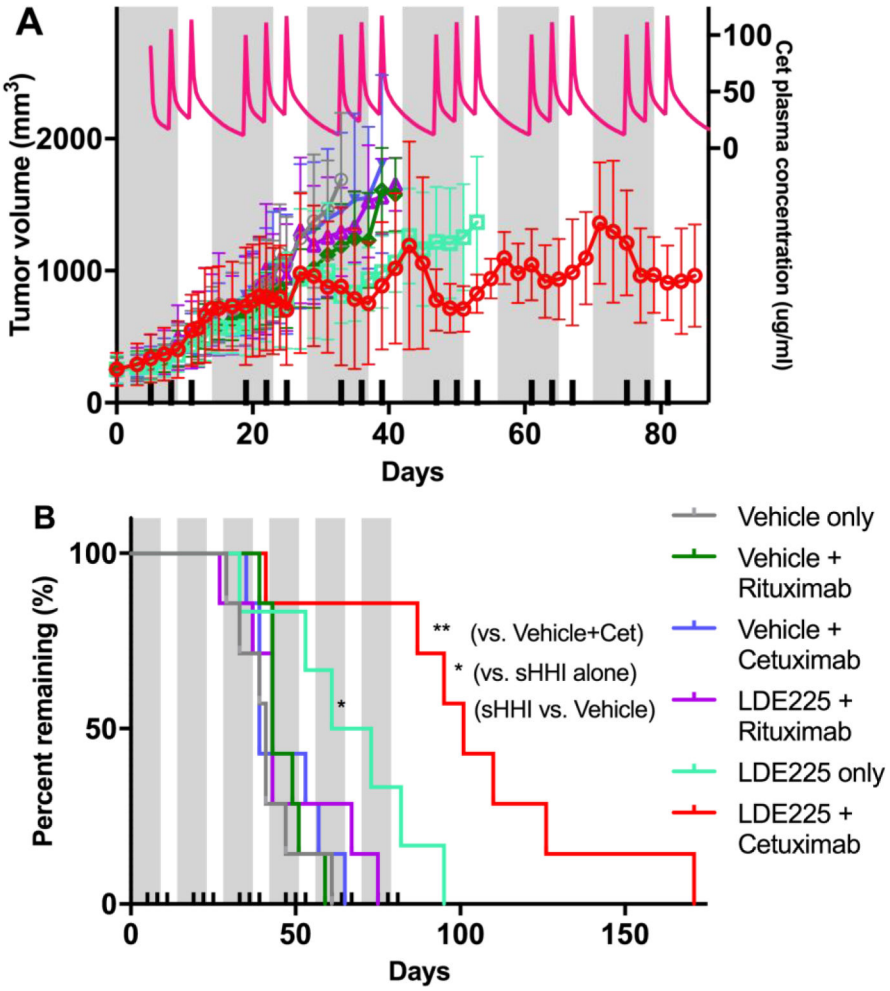

Figure 6. Effect of sequential combination of sHHI and mAb on tumor growth

A, Volume progression of tumor #18269 was measured during multiple treatment cycles consisting of 10d sHHI administration (grey bands; NVP-LDE225 at 40mg/kg/day *p.o.*) with 7mg/kg/dose mAb administered *i.v.* on day 5, 8, and 11 (ticks on abscissa). The interval between sHHI treatment cycles was 4 days. When implanted tumors were 150–500 mm^3 (mean 249.1±99.89 s.d.), mice were randomized into treatment groups having nearly identical means and distributions. Cetuximab was the targeted mAb and rituximab was the non-targeted control mAb. Each group consisted of 7 mice; plots of tumor growth continue until the day that the 2nd of seven mice in a group was removed from study owing to tumor volume progression to the protocol tumor volume limit (TVL). Pink line/right-hand ordinate: Pharmacokinetic model prediction of the cetuximab plasma concentrations resulting from the mAb dosing scheme (see Supplemental Information). **B,** Kaplan Meier analysis of survival time to TVL (2000 mm^3) for each treatment group. Statistical analysis based on Log-rank (Mantel-Cox) and Gehan-Breslow-Wilcoxon tests, as implemented in Prism Graphpad 7. Only the NVP-LDE225-alone (* $p \leq 0.05$) and NVP-LDE225+cetuximab groups (** $p \leq 0.01$) differ statistically from all others. The NVP-LDE225+cetuximab group median survival is significantly greater (* $p \leq 0.05$) than the NVP-LDE225-alone group.